HORIZON EUROPE PROGRAMME

TOPIC HORIZON-CL4-2022-RESILIENCE-01-24

GA No. 101091572

Graphene, MXene and ionic liquid-based sustainable supercapacitor

GREEN CAP

GREENCAP - Deliverable report

D2.1. – Functionalization of SC materials

Funded by the European Union

Deliverable No.	GREENCAP D2.1	
Related WP	WP 2	
Deliverable Title	Functionalization of SC materials	
Deliverable Date	2024-07-15	
Deliverable Type	REPORT	
Dissemination level	Public (PU)	
Author(s)	Artur Ciesielski (UNISTRA)	
Checked by	Name WP leader (UNISTRA)	2024-07-15
Reviewed by (if applicable)	Sebastiano Bellani (BED) Ali Shaygan Nia (TUD)	2024-07-11 2024-07-12
Approved by	Francesco Bonaccorso (BED) - Project coordinator	2024-07-23
Status	Final	2024-07-23

Document History

Version	Date	Editing done by	Remarks
V01	2024-07-11	UNISTRA	
V02	2024-07-11	BED	
V1.0	2024-07-12	TUD	
V1.1	2024-07-15	UNISTRA	

Project summary

GREENCAP project aims to revolutionize the field of energy storage while meeting the EU's climate-neutrality goals and the Action Plan on Critical Raw Materials (CRMs). This multi-disciplinary consortium, consisting of partners from seven European countries and Ukraine, seeks to develop sustainable electrode materials for supercapacitors (SCs) that exhibit battery-like energy density, high power densities, and long cycle life. Utilizing graphene and MXenes as electrode materials and ionic liquids (ILs) for high-voltage electrolytes, GREENCAP will boost the material's specific surface area, ion accessibility, and charge storage while ensuring stability and safety across a wide temperature range. The project will validate this SC technology at an industrial scale (TRL 6) and develop a management system to optimize SC integration into high-end applications and the circular economy.

Publishable summary

The primary objectives of Work Package 2 (WP2) are to enhance the performance of SC electrodes by optimizing material surfaces and interfaces through functionalization and hybridization of electrode materials (EMs), the development of hybrid ionic liquid (IL)/organic solvent electrolytes, and the formulation of IL-pre-intercalated 2D materials. WP2 also focuses on providing fundamental understandings for designing and modelling electrode/electrolyte interfaces and identifying suitable material combinations to boost SC electrode performance. This deliverable specifically relates to objective O2.1, which involves the chemical functionalization of materials developed in WP1 to enhance their electrochemical performance.

This deliverable is organized in four main sections. First, we describe the functionalization of $Ti_3C_2T_x$ MXene with small organic molecules (silane derivatives) through condensation reactions. Using a commercially available silane derivative, 3-aminopropyl)triethoxysilane (APTES), the synthetic conditions are optimized. The results of the functionalization of $Ti_3C_2T_x$ MXene using APTES were successful, achieving the highest level of functionalization in *m*-xylene. Additionally, the synthesis of a novel $Ti_3C_2T_x$ MXene hybrid with ferrocene-APTES (Fc-APTES) molecule is described. The second section describes the functionalization of V_2C MXene using diazonium salts to enhance its K^+-storage performance. The functionalization involved covalently grafting multifunctional azobenzene sulfonic acid (ASA) onto V_2C using 4-aminoazobenzene-4'-sulfonic acid sodium salt. This grafting enhanced the K^+-storage performance of V_2C by introducing redox-active azobenzene units for additional K^+ storage and sulfonate anions for accelerated K^+ diffusion. The ASA-V_2C nanoflakes showed a curved morphology, and high-resolution transmission electron microscopy (HR-TEM) analysis revealed a significant increase in interlayer distance from 0.86 nm to 1.25 nm, indicating successful functionalization. The third section describes the in-situ functionalization of MXene surfaces with borate polyanion groups via a flux-assisted eutectic molten etching approach. The study focused on synthesizing MXenes (Nb_2C and Ti_3C_2) with ordered triatomic-layer borate polyanion terminations (OBO) by co-melting $CuCl_2$ and borax. Electrochemical performance tests showed that OBO-Ti_3C_2 exhibited higher specific capacity and improved cycling stability compared to ClO-Ti_3C_2. DFT calculations and operando SXRD provided insights into the high Li^+ hosting capability and structural evolution of OBO-Ti_3C_2. Finally, the fourth section describes methods to improve the electrochemical performance of graphene-based supercapacitor (SCs) produced by high-pressure homogenization (HPH) and wet-jet milling. These involved N functionalization by adding 1,10-phenanthroline to the synthetic graphite mixture during HPH, followed by heating and characterization, or the CO_2-activiation of heteroatom-doped biochar. Besides, SC electrodes using wet-jet milling (WJM)-produced graphene combined with CO_2-activated biochar from Sargassum algae are presented.

This deliverable successfully achieved its objectives by optimizing the functionalization of MXene and graphene materials and demonstrating improved electrochemical properties. These advancements contribute significantly to the project's overall goal of developing high-performance SC electrodes, providing a solid foundation for future work in electrode material optimization and hybridization. The collaboration between different teams and methodologies highlights the project's comprehensive approach to material innovation and electrochemical performance enhancement.

Contents

List of Figures

List of Tables

Abbreviations & Definitions

Abbreviation	Explanation
2D	Two-dimensional
ABS	Activated biochar derived from Venice lagoon's Sargassum brown macroalgae
AFM	Atomic force microscopy
APTES	(3-aminopropyl)triethoxysilane
ASA	Azobenzene sulfonic acid
BP	Biphenyl
Cg	Gravimetric capacitance
CRM	Critical raw materials
CV	Cyclic voltammetry
DMF	Dimethylformamide
DMSO	Dimethyl sulfoxide
EIS	Electrochemical impedance spectroscopy
EM	Electrode material
Fc-APTES	Ferrocene-(3-aminopropyl)triethoxysilane
FSSCs	Flexible solid-state supercapacitors
FTIR	Fourier transform infrared
GCD	Galvanostatic charge-discharge
GITT	Galvanostatic intermittent titration technique
HPH	High-pressure homogenization
HR-TEM	High-resolution transmission electron microscopy
ILs	Ionic liquids
KFSI	Potassium bis(fluorosulfonyl)imide
Rct	Charge transfer resistance
Rs	Ohmic resistance
SCs	Supercapacitors
SEM	Scanning electron microscopy
TGA	Thermogravimetric analysis
TLC	Thin-layer chromatography
WJM	Wet-jet milling
WP	Work package
XPS	X-ray photoelectron spectroscopy
XRD	X-Ray diffraction analysis

1 Introduction

Supercapacitors (SCs), known for their rapid electron transfer or physical electrostatic adsorption mechanisms, offer higher power densities and superior cyclic stability compared to conventional batteries.[1] They are essential in various applications, including energy recovery, smart grids, consumer electronics, electric vehicles, and solar energy systems. However, SCs face critical challenges including lower energy density compared to batteries (<10 Wh/kg) and limited operating voltage range (<3.0 V). Overcoming these challenges requires the development of novel electrode materials and electrolytes to enhance energy density and ensure environmental sustainability and safety in their applications.[2]

Two-dimensional (2D) materials including MXenes and graphene are pivotal materials for SC electrodes due to their high conductivity, large surface area, and versatile surface chemistry.[3] MXenes, derived from layered transition metal carbides, nitrides, or carbonitrides, possess unique properties such as hydrophilic surfaces and variable surface terminations, enhancing ion transport and conductivity.[4] The chemical modifications of these materials, including functionalization,[5] doping,[6] and hybridization,[7] are crucial for optimizing their electrochemical performance. By increasing the specific surface area through functionalization, graphene, and MXenes provide more active sites for charge storage, thereby enhancing capacitance and energy storage capacity.[8] The tailored electronic properties of functionalized graphene and MXene optimize ionic and electrical conductivity, enabling faster charge/discharge cycles and higher power densities. Moreover, functionalization improves the stability and durability of graphene and MXene electrodes by preventing sheet aggregation and promoting uniform dispersion, which enhances ion accessibility and prolongs cycling life. Overall, functionalized graphene and MXenes hold great potential for revolutionizing SCs, making them more efficient and suitable for various energy storage applications.

2 Functionalization of $Ti_3C_2T_x$ MXene with small organic molecules

UNISTRA conducted the functionalization of $Ti_3C_2T_x$ MXene supplied by TCD. Given that the functional groups present on the surface of $Ti_3C_2T_x$ MXene are primarily -O, -OH, and -F, we selected silane derivatives to conduct a condensation reaction.[9] Initially, we focused our attention on (3-aminopropyl)triethoxysilane (APTES) for the $Ti_3C_2T_x$ MXene functionalization to optimize the synthetic conditions, including type of solvent, duration and temperature of the reaction. The functionalization was performed in solvents of varying polarities to determine in which solvent the degree of functionalization is highest. These solvents included dimethylformamide (DMF), ethanol, methanol, diethyl ether, 1-butanol, 2-propanol, dimethyl sulfoxide (DMSO), and m-xylene. In parallel, UNISTRA performed the synthesis of ferrocene-APTES (Fc-APTES), an electroactive molecule that can be used to functionalize $Ti_3C_2T_x$ MXene through the same mechanism as in the case of APTES. Once the synthetic conditions are optimized, we will extend the functionalization of $Ti_3C_2T_x$ MXene to alkoxysilanes (commercially available) and to Fc-APTES to modulate the interlayer distance of $Ti_3C_2T_x$ MXene as well as to boost the electrochemical performance of pristine $Ti_3C_2T_x$ MXene.

X-ray photoelectron spectroscopy (XPS) analysis was conducted at UNISTRA to determine the degree of $Ti_3C_2T_x$ MXene functionalization by APTES. By normalizing the survey spectra to the Ti element, we found that the highest level of functionalization, in terms of Si atomic percentage, was achieved using m-xylene as the solvent, resulting in a 9.15% functionalization (Table 1 and Figure 1).

The completion of the reaction between APTES and ferrocene was monitored by thin-layer chromatography (TLC) using 3:1 petroleum ether/ethyl acetate as the eluent. Once the reaction was complete, the solvent was removed under vacuum. The crude product was loaded onto Celite and purified by column chromatography, using a gradient of petroleum ether/ethyl acetate from 0 % to 25 % of the polar solvent. The solvent was removed, and the product was isolated as an orange solid with a yield of 50 % (0.95 g). The product was stored under nitrogen at -20°C.

Table 1 Atomic percentage of Si in APTES-functionalized $Ti_3C_2T_x$ MXene.

	Functionalization (%)		
Solvent	**Measurement 1**	**Measurement 2**	**Average**
DMF	5.48	5.40	5.44
Ethanol	3.63	4.36	4.00
Methanol	4.57	3.84	4.21
Diethyl ether	6.20	6.72	6.46
1-butanol	4.38	4.13	4.26
2-propanol	4.03	4.11	4.07
DMSO	5.89	5.83	5.86
m-xylene	8.45	9.84	9.15

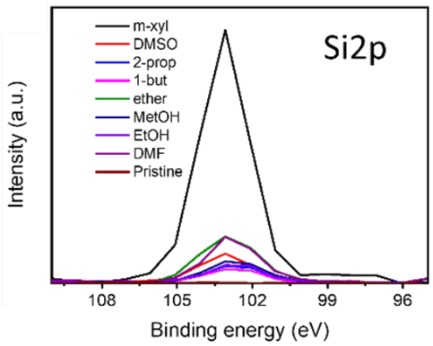

Figure 1. Normalized XPS Si 2p band by conducting the reaction in different solvents.

Structural characterization of $Ti_3C_2T_x$ samples (TCD) was performed by CNR. Self-standing material (aerogel) and as $Ti_3C_2T_x$ powder mechanically adhered on top of glass/ITO and Cu substrates were measured. All samples exhibited the typical (002) reflection of $Ti_3C_2T_x$ MXene (around 6.5°), which corresponds to an interlayer distance of about 1.4 nm (Figure 2). $Ti_3C_2T_x$ aerogel sample only evidences the presence of (008), (103) and (110) diffraction peaks. When the aerogel is mechanically deposited on ITO and Cu, the contributions from the substrate become predominant and only the (002) reflection can still be detected: crystallites in the $Ti_3C_2T_x$ aerogel show a strong preferred orientation along the (002) direction. The attribution of the $Ti_3C_2T_x$ XRD signatures was based on the literature.

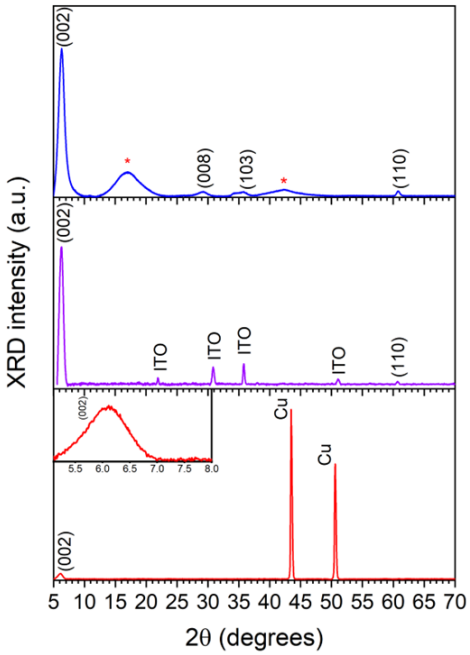

Figure 2. From top to bottom: XRD pattern collected on $Ti_3C_2T_x$ aerogel (blue line) $Ti_3C_2T_x$ on ITO (purple line) and $Ti_3C_2T_x$ on Cu (red line). The reflections labelled by red asterisks are attributed to the sample holder.

CNR started a collaboration with UNISTRA to determine the electronic properties of pristine and functionalized $Ti_3C_2T_x$ samples through photoemission spectroscopy with synchrotron radiation. CNR received samples consisting of pristine $Ti_3C_2T_x$ in the form of aerogel and a film of $Ti_3C_2T_x$ functionalized with APTES deposited on a Cu plate. The core level and valence band analysis of both samples was carried out at room temperature using hν = 750 eV and hν = 50 eV, respectively. The results reported here are preliminary and necessitate further analysis for complete assignment of the core level peaks. Figure 3 reports survey, O 1s, Ti 2p, C 1s, Cl 2p and F Auger spectra of the pristine $Ti_3C_2T_x$ material. The survey spectrum is useful to determine the relative intensities of the different core level lines. The well-defined line shape of the O 1s spectrum can be decomposed into six peaks. The Ti 2p spectrum can be decomposed in three doublets. The doublet at 459.5 eV is related to the presence of minor quantities of TiO_2, while the doublets at lower binding energy are related to $Ti_3C_2T_x$. The peak at 281.9 eV in the C 1s spectrum is also associated to C in $Ti_3C_2T_x$. We observed three doublets in the Cl 2p spectrum. The last spectrum shows the presence of a strong F (KLL) Auger emission.

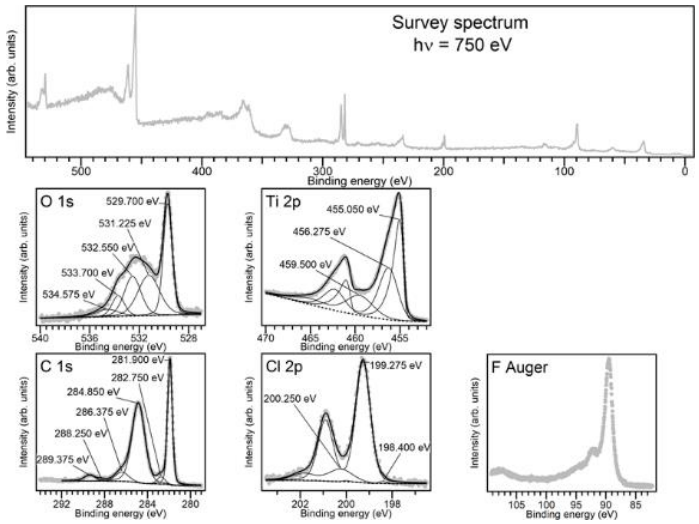

Figure 3. Survey, O 1s, Ti 2p, C 1s, Cl 2p and F Auger spectra of the pristine $Ti_3C_2T_x$ material at hν = 750 eV.

Figure 4 displays the valence band spectra of pristine $Ti_3C_2T_x$. The presence of the Fermi edge clearly demonstrates the metallic character of the material.

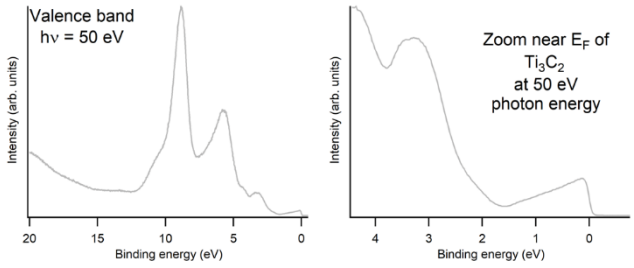

Figure 4. Extended and zoomed valence band spectra of pristine $Ti_3C_2T_x$.

Figure 5 reports survey, O 1s, Ti 2p, N 1s, C 1s, Cl 2p and Si2p + F Auger spectra of the pristine $Ti_3C_2T_x$ material. The survey spectrum is useful to determine the relative intensities of the different core level lines. The well-defined line shape of the O 1s spectrum can be decomposed in six peaks, different from

those of pristine $Ti_3C_2T_x$ in the intensity ratios and the position of the high binding energy peaks. The Ti 2p spectrum can be decomposed in three doublets. In this case, the doublet related to presence of TiO_2 (459 eV) is stronger than in pristine $Ti_3C_2T_x$. The intensity ratio between the doublets at lower binding energy is different from that in pristine $Ti_3C_2T_x$. At variance with pristine $Ti_3C_2T_x$, we can observe two N 1s peaks at 399.975 and 401.85 eV, which demonstrate the functionalization of $Ti_3C_2T_x$. In the C 1s spectrum the component related to $Ti_3C_2T_x$ is much smaller than before the functionalization but remains clearly visible. The Cl 2p spectrum can be fitted with three doublets, in analogy to the case of pristine $Ti_3C_2T_x$. Finally, near the strong F (KLL) Auger emission, we observed the Si 2p line. The two spin-orbit split components of Si 2p are not resolved in the spectrum.

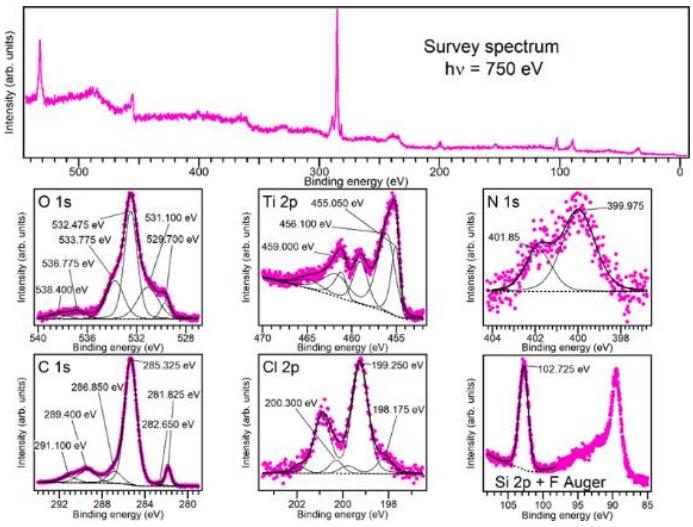

Figure 5. Survey, O 1s, Ti 2p, N 1s, C 1s, Cl 2p and Si2p + F Auger spectra of the pristine $Ti_3C_2T_x$ material at hν = 750 eV.

Figure 6 displays the valence band spectra of functionalized $Ti_3C_2T_x$. The presence of the Fermi edge clearly demonstrates the metallic character of the material also in this case.

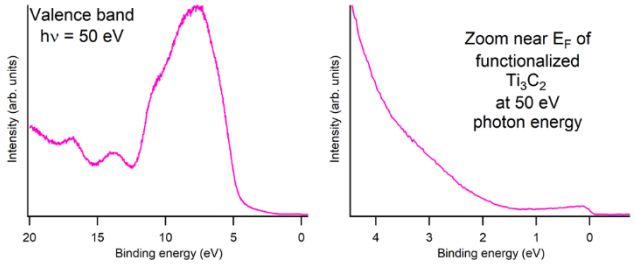

Figure 6. Extended and magnified valence band spectra of functionalized $Ti_3C_2T_x$.

UNISTRA assessed the electrochemical performance of pristine and APTES functionalized $Ti_3C_2T_x$ MXenes by means of cyclic voltammetry (CV), galvanostatic charge discharge (GCD) and electrochemical impedance spectroscopy (EIS) in an asymmetric system with activated carbon as the positive electrode material and (functionalized) $Ti_3C_2T_x$ MXenes as the negative electrode material. Different electrolytes have been supplied by SOLVIONIC and are under evaluation, namely N111TFO (in water, acetonitrile and polycarbonate), Pyr-TFO (in water, acetonitrile and polycarbonate), and N111-TFSI (in acetonitrile and polycarbonate). Conventional sulfuric acid electrolyte was also

employed for the electrochemical performance of MXenes assessment. The electrochemical performance was assessed through GCD at various current densities. The best performance was observed with the aqueous-based electrolytes in all the electrolytes. Figure 7 shows the specific capacitance of $Ti_3C_2T_x$ MXenes as a function of the current density in sulfuric acid, N111-TFO (water) and pyr-TFO (water). Among these electrolytes, sulfuric acid exhibited the highest specific capacitance (250 F/g at 0.1 A/g). The electrochemical characterization of APTES-functionalized $Ti_3C_2T_x$ MXenes is under evaluation.

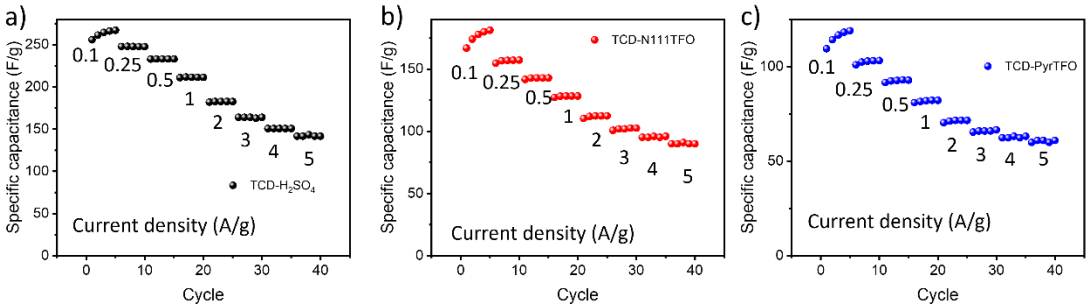

Figure 7. Specific capacitance of $Ti_3C_2T_x$ MXenes as a function of current density in a) sulfuric acid, b) N111-TFO (water) and c) pyr-TFO (water) electrolytes.

3 Functionalization of V_2C MXene with diazonium salts

TUD reported the V_2C MXene functionalization by employing diazonium salts.[10] V_2C was chosen due to its superior chemical stability compared to other M_2X-type MXenes (*e.g.,* Ti_2C and Nb_2C) and classic Ti_3C_2 MXenes, as suggested by the recent theoretical prediction. The covalent grafting of multifunctional azobenzene sulfonic acid (ASA) onto V_2C was achieved using 4-aminoazobenzene-4'-sulfonic acid sodium salt as the starting molecule (Figure 8a), involving amine diazotization and subsequent diazonium removal reactions. Specifically, the amino group of 4-aminoazobenzene-4'-sulfonic acid sodium salt was first converted to a diazonium salt ($-N_2^+Cl^-$) by reacting with $NaNO_2$ and HCl in an ice bat. At the same time, sulfonic acid sodium salt underwent conversion into sulfonic acid in a strong acidic environment. The V_2C dispersion was next added to the yielded diazonium salt solution in an ice bath. When the temperature reached room temperature, the diazonium group dissociated from the molecule, generating radical compounds that subsequently bonded with electronegative surface terminals of V_2C MXene (Figure 8b). The grafted organic molecule was expected to confer multiple benefits to the K^+-storage performance of V_2C). The azobenzene unit exhibits a favourable redox-active nature, enabling the extra K^+-storage site (Figure 8c). The sulfonate anion would act as the desirable K^+-hopping site, accelerating interlayer K^+ diffusion (Figure 8d). The obtained ASA-V_2C nanoflakes display a noticeably curved morphology (Figure 8e). The high-resolution transmission electron microscopy (HR-TEM) was used to evaluate the cross-sectional structure of the ASA- V_2C film (Figure 8f), revealing an interlayer distance of 1.25 nm. This value represents a significant expansion compared to 0.86 nm for the pristine V_2C film (Figure 8g).

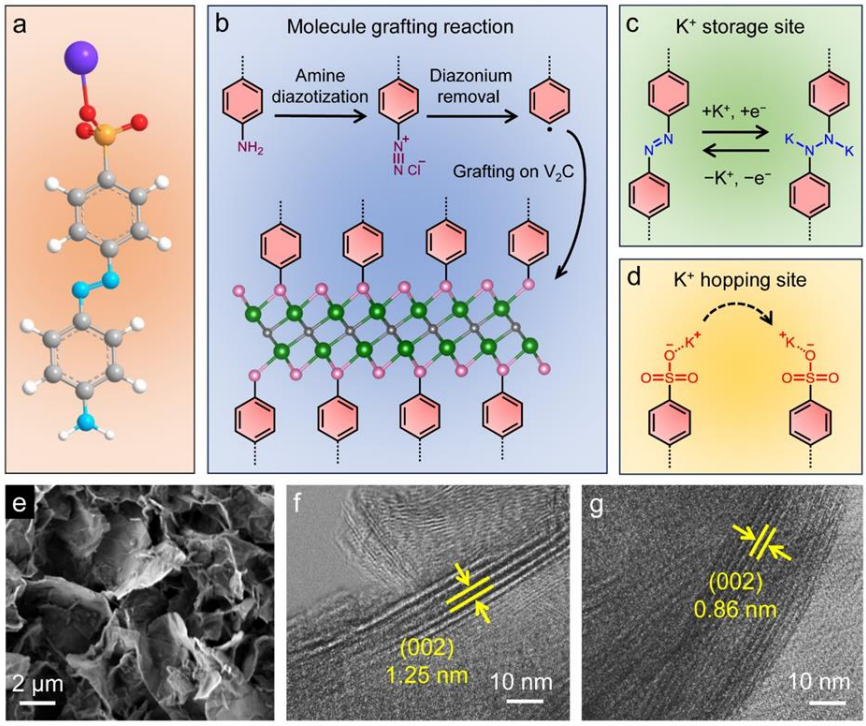

Figure 8. Schematic illustration showing a) 4-aminoazobenzene-4'-sulfonic acid sodium salt (white sphere: H; grey sphere: C; blue sphere: N; orange sphere: S; red sphere: O; purple sphere: Na), b) molecule grafting reaction (black sphere: C; green sphere: V; pin

For comparison, TUD also grafted biphenyl onto V_2C (denoted BP-V_2C) with benzidine as the starting molecule, employing similar amine diazotization and diazonium removal reactions. Thermogravimetric analysis (TGA) for BP-V_2C and ASA-V_2C detected the stable grafting of organic molecules until a high temperature of 259°C (Figure 9**Error! Reference source not found.**a). It is estimated that the organic molecule accounts for 8.3 % and 9.1% of the total weight of BP-V_2C and ASA-V_2C, respectively. Fourier transform infrared (FTIR) spectra further confirmed the successful grafting of organic molecules (Figure 9b). Characteristic peaks of phenyl units, including aromatic C=C stretching (1474 cm^{-1}) and aromatic C-H in-plane bending (1010 and 1086 cm^{-1}, were clearly observed for both BP-V_2C and ASA-V_2C. The peak of ASA-V_2C at 1119 cm^{-1} verifies the presence of sulfonic acid group (-SO_3H stretching, while its N=N stretching (1474 cm^{-1}) overlaps with aromatic C=C stretching. XPS was further conducted on the three samples to evaluate the oxidation of V_2C. In the V 2p XPS spectrum of pristine V_2C (Figure 9c), four deconvoluted peaks can be detected, corresponding to V $2p_{1/2}$ peaks of V^{4+} (523.8 eV) and V^{2+}/V-C (520.9 eV), as well as V $2p_{3/2}$ peaks of V^{4+} (516.3 eV) and V^{2+}/V-C (513.4 eV). The presence of high-valence V^{4+} indicates surface oxidation of V_2C. In comparison with V_2C, ASA-V_2C shows a much weaker V 2p XPS signal (Figure 9**Error! Reference source not found.**d), while the signal is even marginal for BP-V_2C (Figure 9e). This observation suggests dense and homogeneous coverage of functional molecules on the V_2C surface. Following 20 keV Ar^+ cluster sputtering for 5 min, the V 2p signal intensity of BP-V_2C and ASA-V_2C becomes substantially enhanced. Both BP-V_2C and ASA-V_2C show dominant V^{2+}/V-C peaks, and their high-valence V^{4+} peaks are considerably suppressed. This result reflects the effective role of the grafted molecules in inhibiting surface oxidation of V_2C. Furthermore, Figure 9f compares the X-Ray diffraction analysis (XRD) patterns of pristine V_2C, BP-V_2C, and ASA-V_2C. The characteristic (002) peak undergoes a clear negative shift from V_2C (10.3°) to BP-V_2C (7.9°) and ASA-V_2C (7.1°), indicating the gradual expansion of the interlayer distance. Based on Bragg's Law, d-spacings were determined to be 0.86, 1.12, and 1.25 nm for V_2C, BP-V_2C, and ASA-V_2C, respectively. These results are in good agreement with the measured interlayer

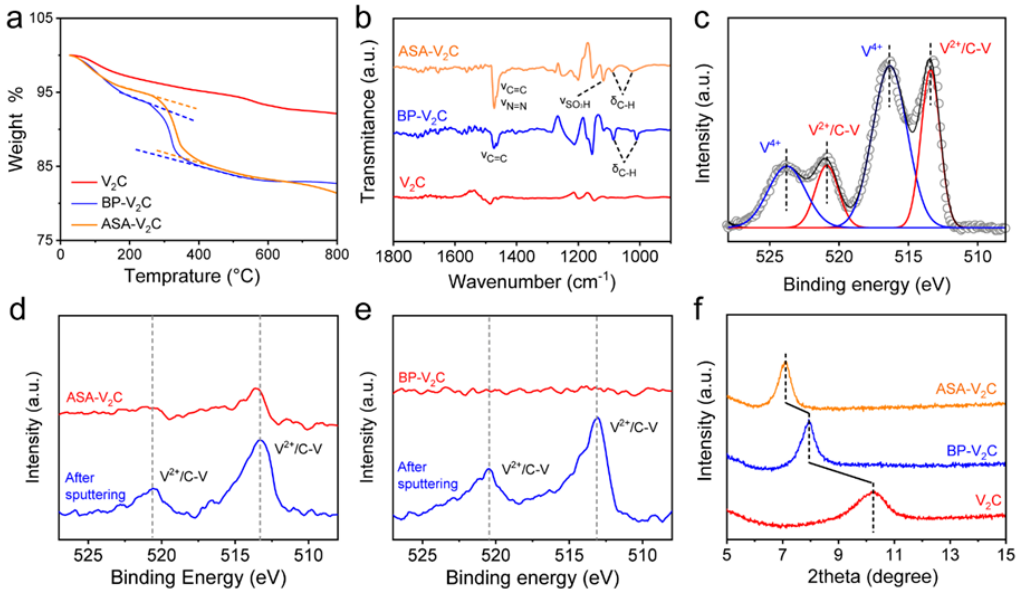

Figure 9. a) TGA and b) FTIR spectra of V_2C, BP-V_2C, and ASA-V_2C. V 2p XPS spectra of c) V_2C, d) BP-V_2C, and e) ASA-V_2C. f) XRD patterns of V_2C, BP-V_2C, and ASA-V_2C.

distance in HR-TEM images.

TUD investigated the performance of organic molecules functionalization MXene electrode for K^+ storage. The K^+-storage performance of free-standing V_2C, BP-V_2C, and ASA-V_2C films was evaluated in two-electrode Swagelok cells with an electrolyte of 5 M potassium bis(fluorosulfonyl)imide (KFSI) dissolved in a mixture of dimethyl carbonate and ethylene carbonate (1:1 vol.%). Figure 10a compares the CV curves of the three electrodes at 0.5 mV s^{-1} Apparently, ASA-V_2C presents the largest CV area among the three electrodes, indicating its superior K^+-storage capacity.

To assess the rate capability of the three electrodes, GCD curves were collected at various current densities ranging from 0.05 to 20 A g^{-1} (Figure 10b). As depicted in Figure 10c, the ASA-V_2C electrode exhibits a remarkable specific capacity of 173.9 mAh g^{-1} at 0.05 A g^{-1}, greatly surpassing the specific capacities of the V_2C electrode (121.5 mAh g^{-1}) and the BP-V_2C electrode (136.9 mAh g^{-1}). Of significant note, at a significantly increased current density of 20 A g^{-1} (referring to a short charge/discharge time of approximately 13.5 s), the ASA-V_2C electrode maintains a decent specific capacity of 74.9 mAh g^{-1}, equivalent to 43.1 % of its maximum specific capacity. In contrast, the V_2C electrode and the BP-V_2C electrode at 20 A g^{-1} only exhibit capacity retention of 12.0% and 17.4%, respectively (Figure 10c). Specific capacities as a function of charge/discharge time were further plotted for the ASA-V_2C electrode (Figure 10d), highlighting the state-of-the-art performance in comparison with recently reported K^+-storage MXene anodes, such as V_2C, Ti_3CN, alkalized Ti_3C_2, and Ti_3C_2 nanoribbons. EIS was performed on the three electrodes at various potentials to gain insights into the performance improvement induced by the grafted molecules. The values of Ohmic resistance (R_s) and charge transfer resistance (R_{ct}) for the three electrodes (Figure 10e) were derived by fitting the EIS data with an equivalent circuit. Across all potentials, R_s follows the trend of V_2C > BP-V_2C > ASA-V_2C, suggesting that the grafted molecule effectively enhance the charge transport capability of V_2C. Moreover, the significantly improved charge transfer of ASA-V_2C was evident from its pronouncedly lower R_{ct} (38.0 Ω at 0.05 V vs. K^+/K) in comparison with V_2C (110.8 Ω at 0.05 V vs. K^+/K) and BP-V_2C (99.6 Ω at 0.05 V vs. K^+/K). In addition, K^+ diffusion coefficient (D) of the three electrode was quantified using the galvanostatic intermittent titration technique (GITT, Figure 10f). As expected, ASA-V_2C demonstrates the fastest K^+ diffusion with D values of 1.2×10^{-9} ~ 1.6×10^{-8} cm^2 s^{-1}, significantly outclassing V_2C (1.6×10^{-11} ~ 1.4×10^{-9} cm^2 s^{-1}) and BP-V_2C (2.0×10^{-11} ~ 2.0×10^{-9} cm^2 s^{-1}). All these results underscore the significant role of sulfonate anions equipped on the grafted molecules in accelerating K^+ diffusion between V_2C layers.

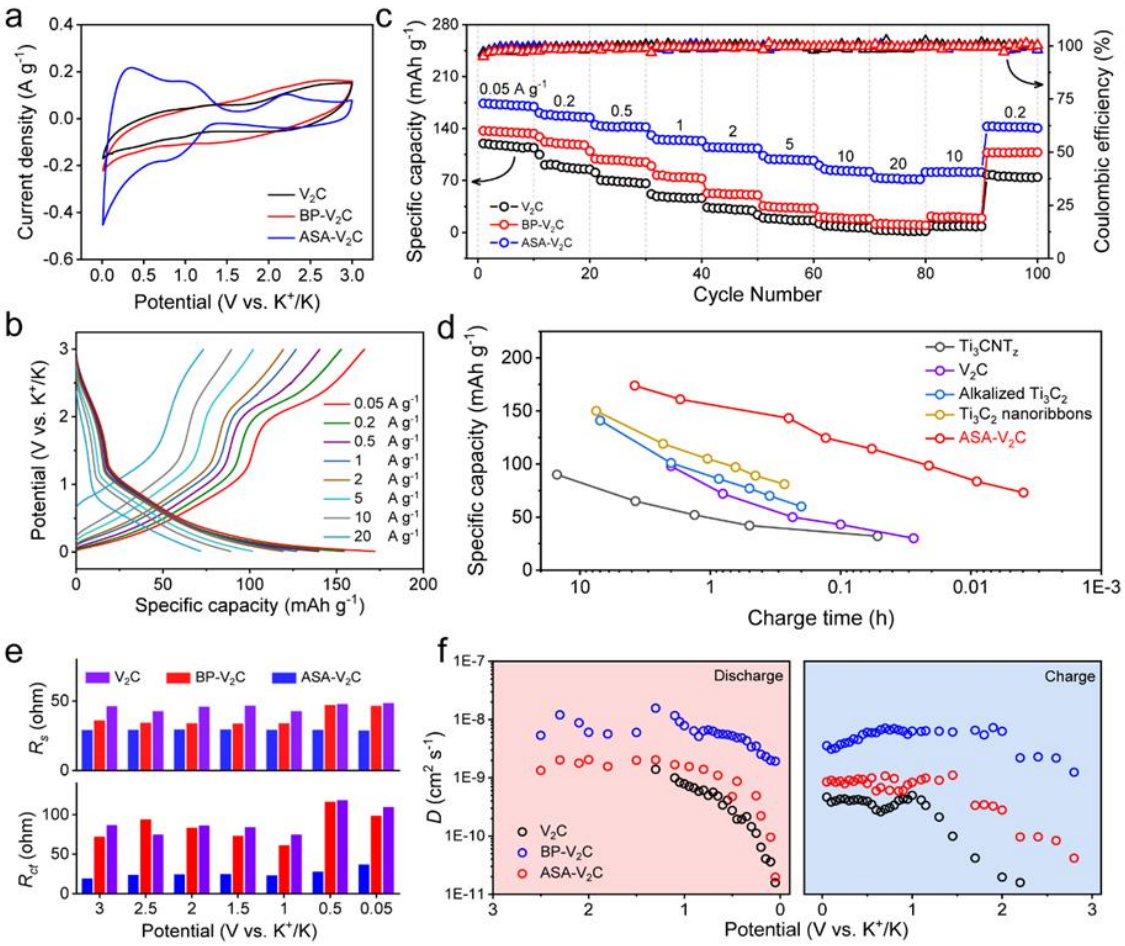

Figure 10. a) CV curves at 0.5 mV s^{-1} and b) rate performance of the V_2C, BP-V_2C, and ASA-V_2C electrodes. c) GCD profiles of the ASA-V_2C electrode at various current densities. d) Specific capacity as a function of charge time for the ASA-V_2C electrode in comparison with recently reported K^+-intercalation MXene electrodes. e) R_s and R_{ct} of the V_2C, BP-V_2C, and ASA-V_2C electrodes derived from the EIS measurements. f) K^+ diffusion coefficients of the V_2C, BP-V_2C, and ASA-V_2C electrodes calculated from the GITT measurements.

4 *In-situ* functionalization of the surface of MXene materials with borate polyanion groups through a flux-assisted eutectic molten etching approach

TUD studied ordered triatomic-layer borate polyanion terminations.[11] MXenes are commonly synthesized *via* the selective removal of A-layers from layered ternary metal carbides/nitrides (that is, MAX). Although the $M_{n+1}X_n$ backbone of MXene is inherited from MAX precursors, terminations are predominantly determined by the synthetic process. Typically, wet-chemistry etching utilizing fluorine- or chlorine-containing aqueous acids yields MXenes with randomly mixed –OH, –O, –F and –Cl terminations. Lewis-acid molten salt etching shows promise in producing MXenes with monoatomic-layer halogen terminations (–Cl, –Br or –I). These halogen terminations can be subsequently substituted with chalcogen terminations or other monoatomic-layer terminations (for example, lead and antimony) by a post-conversion process. However, these terminations are susceptible to oxidation upon air exposure or during washing steps and thus fall short in stabilizing the ordered termination structure. Furthermore, other synthetic approaches (for example, hydrothermal etching electrochemistry and iodine-assisted etching and post-treatment strategies (for example, annealing and chemical conversion) offer termination manipulation, yet termination options remain constrained to the aforementioned types. Critically, the instability and disordering of the termination structure pose a major challenge for MXene applications that necessitate structural integrity and superior quality. We showcased the synthesis of MXenes (Nb_2C and Ti_3C_2) with ordered triatomic-layer borate polyanion terminations, using a flux-assisted eutectic molten etching approach. The synthesis involves co-melting $CuCl_2$ and borax ($Na_2B_4O_7{\cdot}10H_2O$), whereupon $CuCl_2$ selectively removes aluminium layers from MAX phases, while thermally decomposed borax generates BO_2^- species that cap the MXene surface (denoted OBO terminations, Figure 11).

Scanning electron microscopy (SEM) images reveal the typical accordion-like morphology of OBO-Ti_3C_2 (Figure 11a) and OBO-Nb_2C. Pristine borax was annealed under the same conditions used for MXene preparation to identify its decomposition products (borax-A). In contrast to the two characteristic ^{11}B NMR signals of borax at 2.3 and 17.4 ppm, borax-A presents two signals at 1.1 and 15.3 ppm (Figure 11b), corresponding to the locally tetrahedrally oxygen-coordinated boron atom ($B(OR)_4$) and the threefold oxygen-coordinated boron atom ($B(OR)_3$), respectively. These two signals align with those of standard B_2O_3 and $NaBO_2$, which verifies the thermal decomposition of borax outlined. High-resolution B 1*s* X-ray photoelectron spectroscopy (XPS) spectra of both OBO-Ti_3C_2 and OBO-Nb_2C (Figure 11c) present a broad peak at 191.5 eV, matching with the binding energy of $NaBO_2$. This suggests that the boron atoms in OBO terminations have a similar electronic state to the boron atoms in $NaBO_2$, suggesting that OBO terminations originate from BO_2^- species.

For comparison, TUD also synthesized ClO-Ti_3C_2 and ClO-Nb_2C with mixed and disordered chlorine/oxygen terminations using a previously reported method. In the metal (Ti, Nb) K-edge X-ray absorption near-edge structure (XANES) spectra, both OBO-Ti_3C_2 (Figure 11d) and OBO-Nb_2C present a similar spectrum shape to their corresponding metal carbide references (that is, TiC and NbC). The absorption edge energy (E_0) of OBO-MXenes is higher than that of the corresponding chlorine/oxygen-terminated MXene counterparts, which indicates that OBO terminations induce higher oxidation states in the surface metal atoms of MXenes. Additionally, metal (Ti, Nb) K-edge Fourier-transformed extended X-ray absorption fine structure (EXAFS) *R*-space spectra were performed to reveal the local

coordination of metal atoms in OBO-MXenes. The visualized wavelet-transform analysis of EXAFS in *R* and *k* spaces was carried out for OBO-Ti_3C_2 (Figure 11e-h) and OBO-Nb_2C , and the results are compared with the corresponding chlorine/oxygen-terminated MXenes, metal carbides and metal oxides. The contour intensity in the analysis revealed two maxima for both OBO-Ti_3C_2 and OBO-Nb_2C, which correspond to the first-shell metal–carbon/oxygen scattering (1.60 Å for Ti–C/O, 1.63 Å for Nb–C/O in *R* space) and second-shell metal–carbon–metal scattering (2.74 Å for Ti–C–Ti, 2.73 Å for Nb–C–Nb in *R* space). The first-shell metal–carbon/oxygen scatterings in OBO-Ti_3C_2 and OBO-Nb_2C are slightly lower in *R* space than in ClO-Ti_3C_2 (1.71 Å) and ClO-Nb_2C (1.70 Å), reflecting their relatively compact

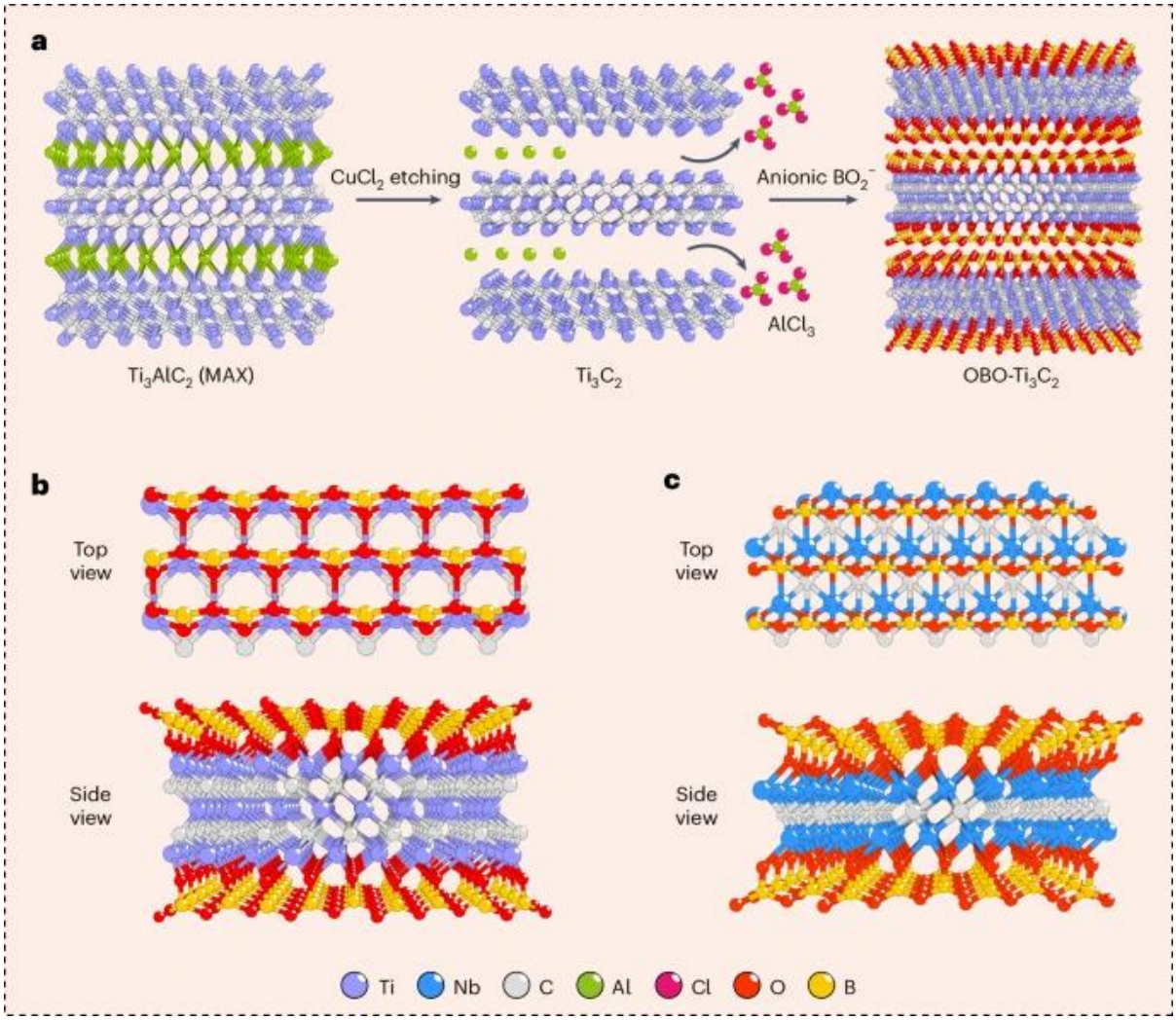

metal-termination connecting bonds.

Figure 11. a–c) Schematics showing the synthesis process with a) Ti_3C_2 MXene as an example and b) atomic structures of OBO-Ti_3C_2 and c) OBO-Nb_2C.

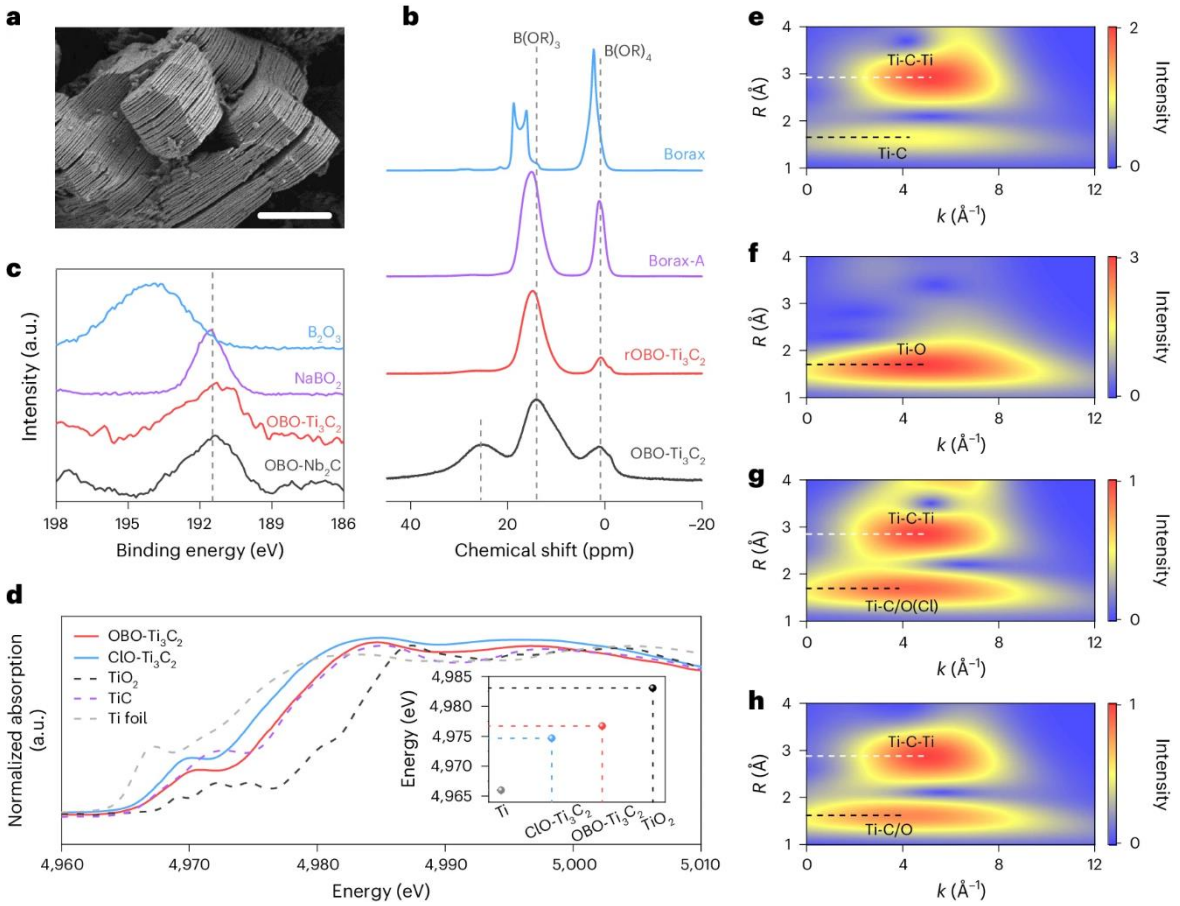

Figure 12. a) SEM image of OBO-Ti_3C_2. Scale bar, 2 µm. b) Solid-state ^{11}B MAS NMR spectra of borax, borax-A, rOBO- Ti_3C_2 and OBO- Ti_3C_2. c) B 1s XPS spectra of B_2O_3, $NaBO_2$, OBO- Ti_3C_2 and OBO-Nb_2C. d) XANES spectra of ClO- Ti_3C_2, OBO- Ti_3C_2 and the corresponding TiO_2, TiC and Ti foil references. Inset: comparison of corresponding edge energy (E0) position. The E0 values are derived for OBO-Ti_3C_2 (4,976.7 eV), ClO- Ti_3C_2 (4,974.7 eV), OBO-Nb_2C (19,001.6 eV) and ClO-Nb_2C (19,000.5 eV). e–h) Contour plots of the wavelet-transformed EXAFS of e) TiC, f) TiO_2, g) ClO-Ti_3C_2 and h) OBO-Ti_3C_2.

TUD also investigated the effect of OBO terminations on the charge-storage properties of Ti_3C_2. The electrochemical performance of OBO-Ti_3C_2, and of ClO-Ti_3C_2 as a control sample, was evaluated in 1 M $LiPF_6$. Figure 13a presents the cyclic voltammetry curves of OBO-Ti_3C_2 and ClO-Ti_3C_2 electrodes at 0.5 mV s^{-1} after activation. Galvanostatic charge–discharge curves of the two electrodes at various current densities were collected to quantify the specific capacity. Both the OBO-Ti_3C_2 electrode (Figure 13b) and the ClO-Ti_3C_2 electrode exhibit slope-shaped profiles without apparent plateau. Of note, the OBO-Ti_3C_2 electrode delivers a maximum specific capacity of 420 mAh g^{-1} (1,512 C g^{-1}) at 50 mA g^{-1}.

TUD further sought insights into the high Li^+-hosting capability of OBO-Ti_3C_2 through DFT calculations. Specifically, we simulated the absorption of Li^+ on two different sites of OBO-Ti_3C_2 using a 2 × 2 supercell with a formula of $Ti_{3x}C_{2x}B_{2x}O_{4x}$. The absorption begins with the site inside the OBO cage (site-1), followed by the site located on the top of the outer oxygen layer (site-2) (Figure 12c). In addition, OBO terminations contribute to the prolonged cycling stability of Ti3C2 MXene. In a cycling test at 0.1 A g^{-1} for 550 cycles (Figure 12d), the OBO-Ti_3C_2 electrode exhibits a capacity retention of 98%, in stark contrast to the capacity retention of the ClO-Ti_3C_2 electrode (59%). Moreover, the OBO-

Ti_3C_2 electrode retains 94% of its original capacity after 2,000 cycles at 1 A g^{-1}, whereas the ClO-Ti_3C_2 electrode maintains 79% of the original capacity (Figure 12e). Operando SXRD was employed to monitor the structural evolution of OBO-Ti3C2 during Li+ intercalation/deintercalation (Figure 12f).

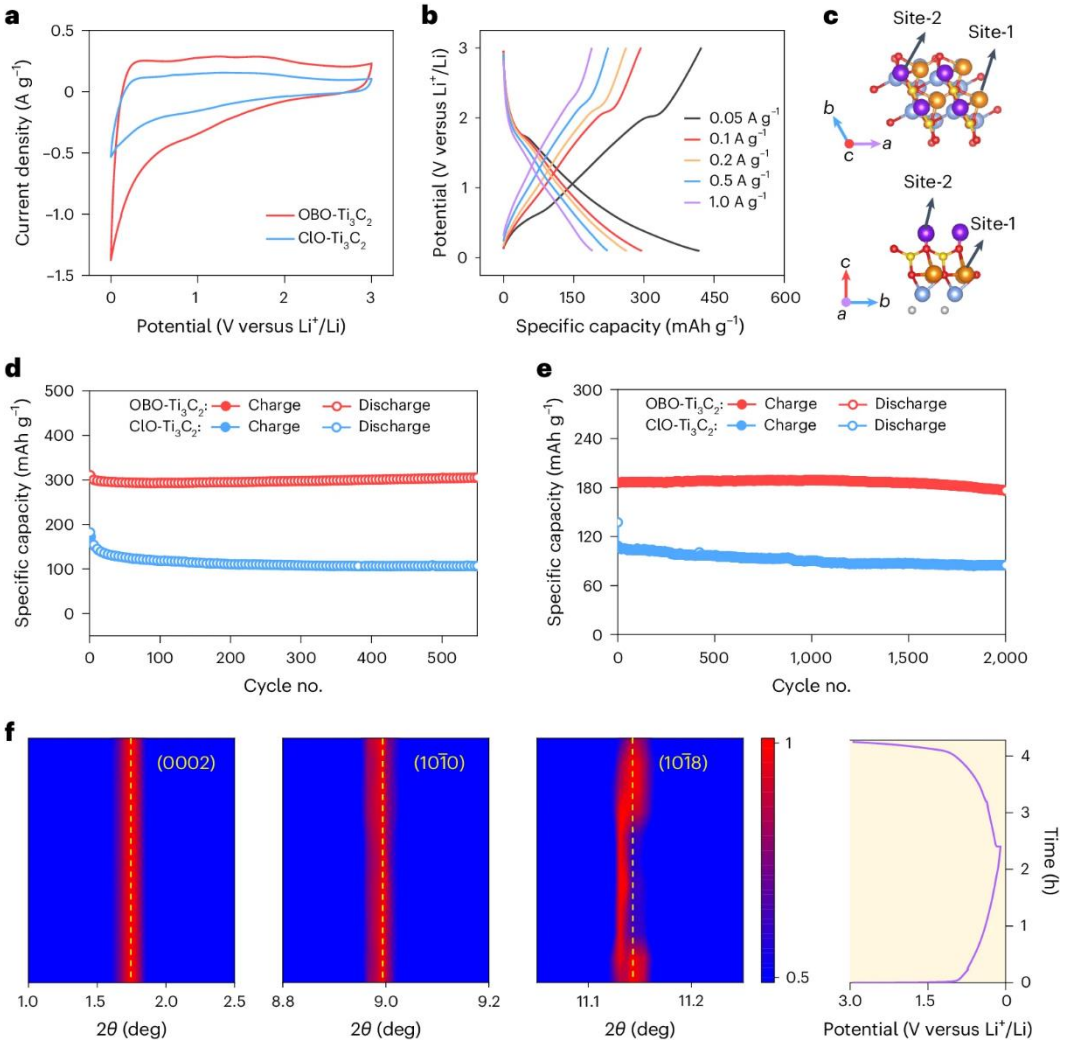

Figure 13. a), Cyclic voltammetry profiles of OBO-Ti_3C_2 and ClO-Ti_3C_2 electrodes at 0.5 mV s^{-1}. b), Galvanostatic charge–discharge profiles of the OBO-Ti_3C_2 electrode at various current densities. c), Li^+-adsorption configurations of OBO-Ti_3C_2. Blue spheres, titanium; grey spheres, carbon; yellow spheres, boron; red spheres, oxygen, purple spheres, site-1 lithium; orange spheres, site-2 lithium. d,e), Cycling stability of the OBO-Ti_3C_2 and ClO-Ti_3C_2 electrodes at 0.1 A g^{-1} (d) and 1 A g^{-1} (e). f), Voltage profile and contour plots of operando SXRD of the OBO-Ti_3C_2 electrode, showing a characteristic (0002) peak at 1.74°, a (101$^-$0) peak at 8.99° and a (101$^-$8) peak at 11.13°.

5 Nitrogen doping of few-layer graphene

To improve the electrochemical performance of supercapacitors made using graphene produced by high-pressure homogenization (HPH), a method to perform N functionalization or doping was developed by UCAM, compatible with the high throughput nature of HPH, see Figure 14. This involves adding N-containing aromatic compounds into the synthetic graphite mixture during HPH. 1,10-Phenanthroline is chosen as the N-containing aromatic compound because it binds well to graphene and has high solubility in solvents used in HPH. KS25 synthetic graphite was mixed with 5 wt% ethyl cellulose and 10 wt% 1,10-phenanthroline in isopropanol and run through the HPH for 50 cycles using a 100 µm microfluidic channel. The resultant mixture was then heated at 800 °C for 30 minutes, then characterized and used to fabricate SC electrodes.

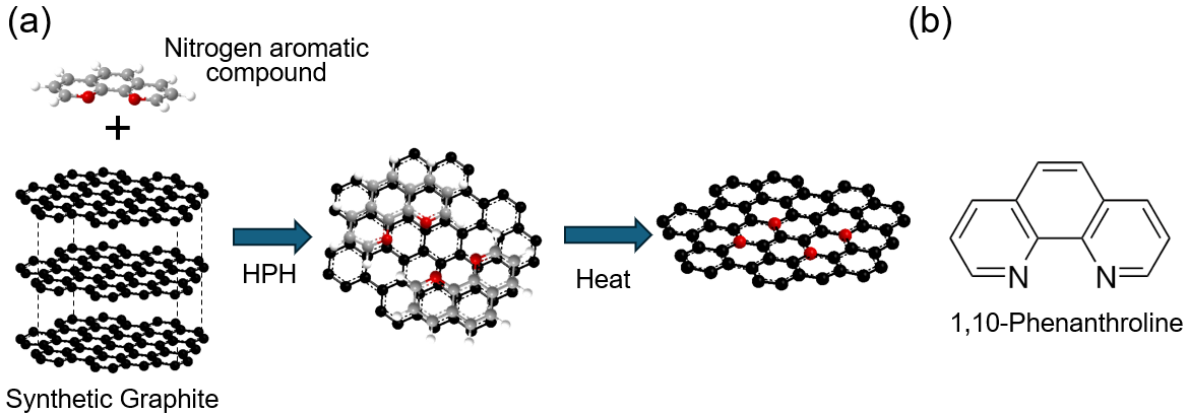

Figure 14. a) N doping procedure. B) Structure of N-containing aromatic compound used.

N-doped graphene was characterized by UCAM using scanning electron microscopy (SEM), atomic force microscopy (AFM) and four-point probe conductivity, see Figure 15. SEM shows that the flake size and thickness is reduced compared to synthetic graphite (20µm and 100 nm, respectively) (Figure 12a,b) down to an average of (7.5 µm and ~22 nm, respectively) (Figure 12c, d). An ink was also formulated and conductivity measurements using a four-point probe done, giving R_S~6 Ω/□ for a thickness~10 µm.

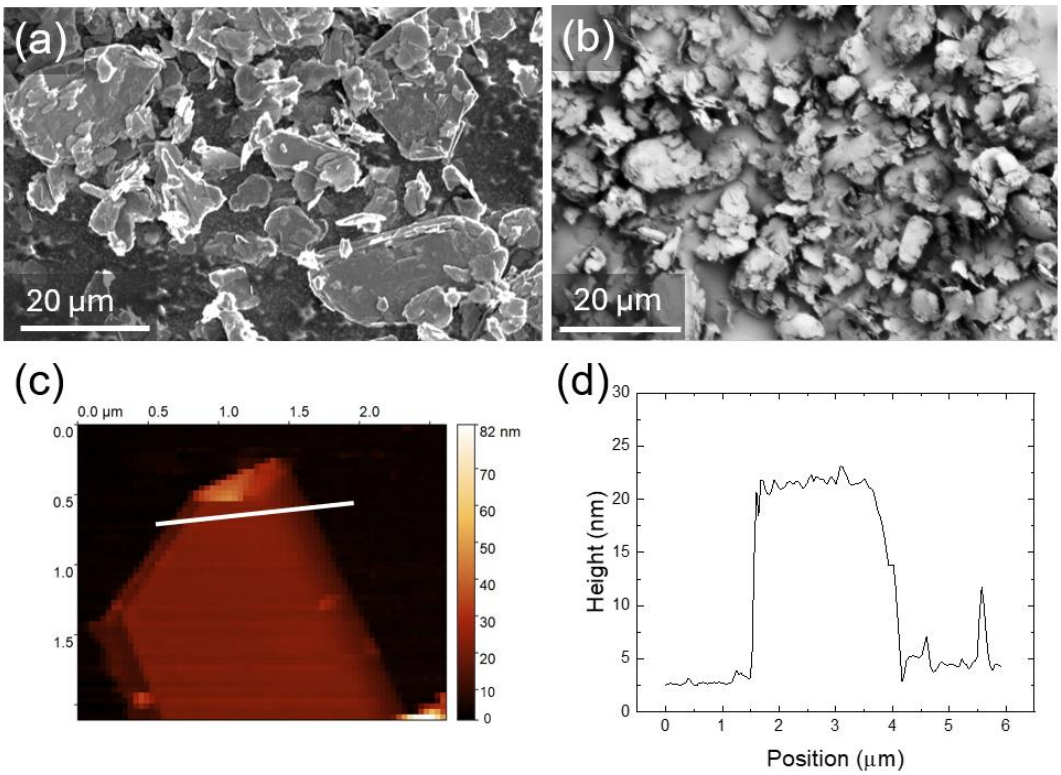

Figure 15. SEM images of a) synthetic graphite and b) nitrogen-doped graphene. c) AFM image and d) cross-section height profile of a nitrogen-doped graphene flake.

In parallel, BED attempted the functionalization of pristine few-layer graphene, produced by proprietary wet-jet milling (WJM) exfoliation, and curved graphene, supplied by SM, by means of bio-approach, which was however detrimental for the electrochemical performances. In addition, BED developed SC electrodes coupling WJM-produced few-layer graphene with heteroatoms doped graphitic materials produced by CO_2-activation of biochar derived from Venice lagoon's Sargassum brown macroalgae (activated product named ABS).[12] The CO_2 activation (at 800 °C, for 1, 1.5 or 2 hours) of WJM-produced FLG marginally increased the capacitive performance of starting materials, pointing out the difficulties to activate pristine graphene. ABS was used as active material in combination with our WJM-produced as conductive additives (electrochemical tests carried out in aqueous and organic supercapacitors (Figure 16), as well as flexible solid-state supercapacitors (FSSSCs) (Figure 17). These preliminary results will be extended to devices using IL-based electrolytes, including protic ones (recently supplied by SOLV), which are more promising for the effective exploitation of pseudocapacitive effects involving heteroatoms functionalities.

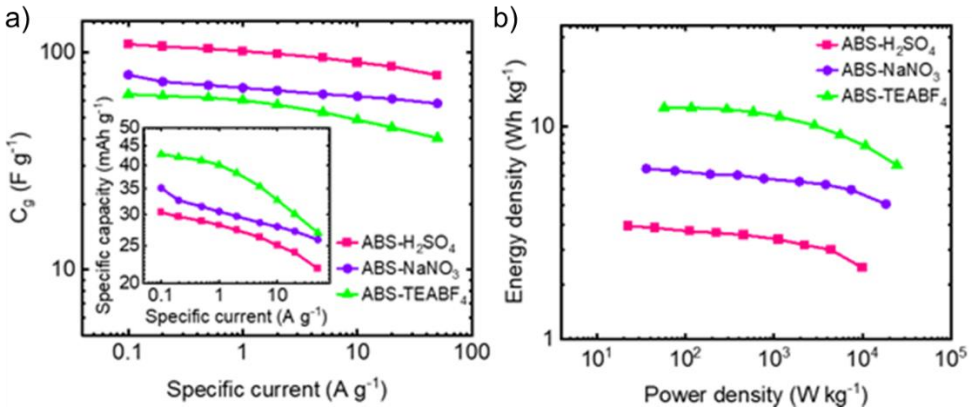

Figure 16. a) Electrode C_g (inset, specific capacity) measured for the investigated ABS-based EDLCs as a function of the specific current (data extrapolated from the galvanostatic charge/discharge profiles). b) Ragone plots. Electrolytes: 1 M H_2SO_4; 8 M $NaNO_3$; 1 M $TEABF_4$ in ACN.

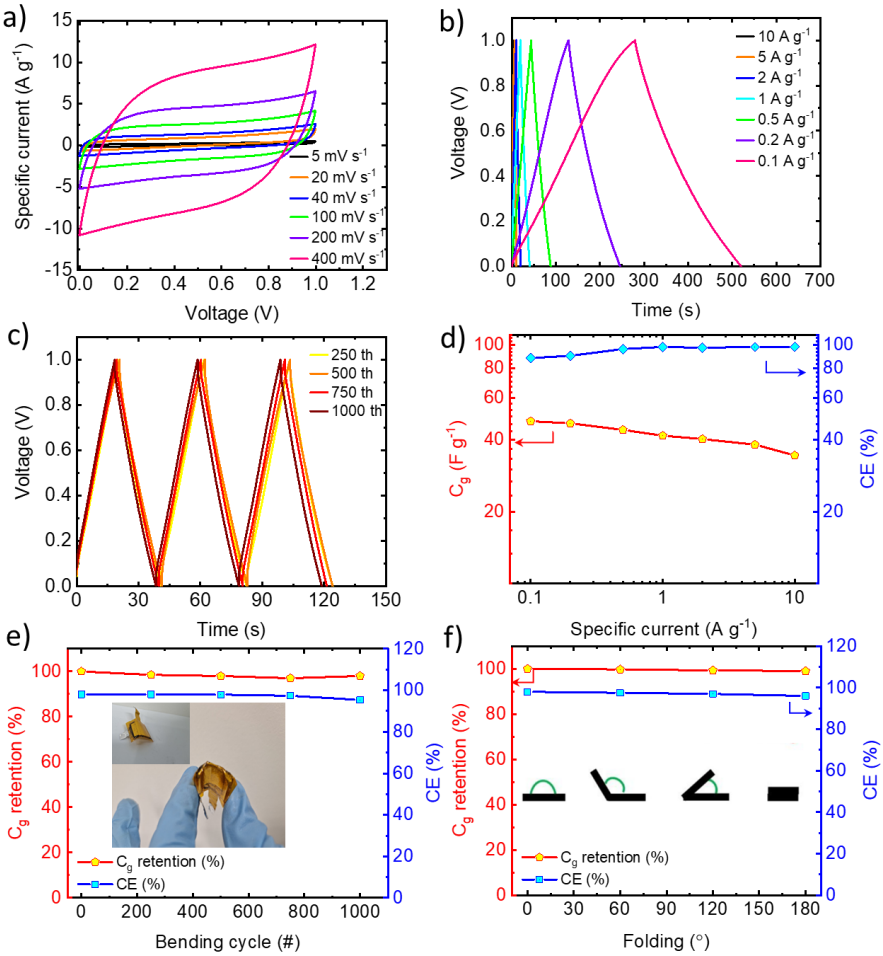

Figure 17. Electrochemical characterization of the ABS-based FSSSC. a) CV curves measured at different voltage scan rates, ranging from 5 to 400 mV s^{-1}, b) GCD profiles measured at various specific currents, ranging from 0.1 to 10 A g^{-1}. C) C_g and CE as function of the specific current. d) GCD profiles measured after 250, 500, 750, and 1000 bending cycles at 1 A g^{-1} (curvature radius = 2 cm). e) C_g retention and CE of the FSSSC over 1000 bending cycles. f) C_g retention and CE of the FSSSC folded at 0°, 60°, 120°, and 180°.

Conclusion and Recommendation

In conclusion, the functionalization of $Ti_3C_2T_x$ MXene with APTES at UNISTRA has demonstrated significant advancements in enhancing the material's properties for potential supercapacitor applications. XPS analysis confirmed a high degree of functionalization, achieving 9.15% Si atomic percentage on the $Ti_3C_2T_x$ surface. This functionalization strategy offers improved control over surface chemistry, crucial for optimizing electrochemical performance. Collaboration with CNR also provided insights into the structural and electronic changes induced by APTES functionalization, showcasing potential benefits in terms of stability and conductivity. Further electrochemical evaluations using various electrolytes have shown promising results, suggesting enhanced specific capacitance. TUD successfully performed the functionalization of V_2C MXene using diazonium chemistry to graft ASA and BP molecules onto its surface. Characterization techniques confirmed successful grafting, altering the MXene structure with ASA-V_2C displaying a curved morphology and expanded interlayer spacing compared to pristine V_2C. ASA-V_2C exhibited superior potassium-ion storage performance over V_2C and BP-V_2C, attributed to the redox activity of azobenzene and sulfonate groups facilitating K^+ diffusion. TUD successfully synthesized MXenes (Nb_2C and Ti_3C_2) with ordered triatomic-layer borate polyanion terminations using a flux-assisted eutectic molten etching approach. This method provides superior stability and structural integrity compared to traditional etching methods. OBO-terminated MXenes exhibited higher oxidation states and improved local coordination, leading to enhanced electrochemical performance, including a maximum specific capacity of 420 mAh/g and superior cycling stability. UCAM demonstrated via SEM and AFM the successful N-doping and morphology changes of graphene produced via HPH, validating the method's efficacy in preparing N-doped graphene for superior SCs electrodes. Lastly, BED attempted various functionalization processes for the WJM-produced graphene and other graphitic active materials. Heteroatom-doping followed by CO_2 activation resulted beneficial to improve the electrochemical performances of carbon-based SCs in different types of electrolytes, as well as in FSSCs.

6 Risks and interconnections

6.1 Risks/problems encountered

No risks have arisen related to this deliverable.

Risk No.	What is the risk	Probability of risk occurrence[1]	Effect of risk[1]	Solutions to overcome the risk
WP2	Low functionalization degree (<10%) of CRM-free MXenes	Medium	Medium-low	Systematic screening of ratio MXene/organic molecule within the reaction mixture. Addition of catalysts, pH adjustments.

[1)] Probability risk will occur: 1 = high, 2 = medium, 3 = Low

6.2 Interconnections with other deliverables

N/A

7 Deviations from Annex 1

There are no deviations from the description of this deliverable as given in Annex I of the GA.

8 References

[1] B. K. Kim, S. Sy, A. Yu, J. Zhang, in *Handbook of Clean Energy Systems*.
[2] M. Tomy, A. Ambika Rajappan, V. Vm, X. Thankappan Suryabai, *Energy & Fuels* **2021**, 35, 19881.
[3] a)Y. Chen, H. Yang, Z. Han, Z. Bo, J. Yan, K. Cen, K. K. Ostrikov, *Energy & Fuels* **2022**, 36, 2390; b)A. Velasco, Y. K. Ryu, A. Boscá, A. Ladrón-de-Guevara, E. Hunt, J. Zuo, J. Pedrós, F. Calle, J. Martinez, *Sustainable Energy & Fuels* **2021**, 5, 1235.
[4] Y. Gogotsi, B. Anasori, *ACS Nano* **2019**, 13, 8491.
[5] L. Dai, *Acc. Chem. Res.* **2013**, 46, 31.
[6] F. Han, W. Jing, Q. Wu, B. Tian, Q. Lin, C. Wang, L. Zhao, J. Liu, Y. Sun, Z. Jiang, *J. Power Sources* **2022**, 520, 230866.
[7] F. Bonaccorso, L. Colombo, G. Yu, M. Stoller, V. Tozzini, A. C. Ferrari, R. S. Ruoff, V. Pellegrini, *Science* **2015**, 347, 1246501.
[8] C. Valentini, V. Montes-García, A. Ciesielski, P. Samorì, *Adv. Sci* **2024**, 11, 2309041.
[9] I. Janica, V. Montes-García, F. Urban, P. Hashemi, A. S. Nia, X. Feng, P. Samorì, A. Ciesielski, *Small Methods* **2023**, 7, 2201651.
[10] D. Sabaghi, J. Polčák, H. Yang, X. Li, A. Morag, D. Li, A. S. Nia, S. Khosravi H, T. Šikola, X. Feng, M. Yu, *Adv. Energy Mater.* **2024**, 14, 2302961.
[11] D. Li, W. Zheng, S. M. Gali, K. Sobczak, M. Horák, J. Polčák, N. Lopatik, Z. Li, J. Zhang, D. Sabaghi, S. Zhou, P. P. Michałowski, E. Zschech, E. Brunner, M. Donten, T. Šikola, M. Bonn, H. I. Wang, D. Beljonne, M. Yu, X. Feng, *Nature Materials* **2024**.
[12] A. Bagheri, S. Taghavi, S. Bellani, P. Salimi, H. Beydaghi, J. K. Panda, M. Isabella Zappia, V. Mastronardi, A. Gamberini, S. Balkrishna Thorat, M. Abruzzese, L. Pasquale, M. Prato, M. Signoretto, X. Feng, F. Bonaccorso, *Chem Eng J* **2024**, 496, 153529.

9 Acknowledgement

The author(s) would like to thank the partners in the project for their valuable comments on previous drafts and for performing the review.

Project partners:

#	Partner short name	Partner Full Name
1	BED	BEDIMENSIONAL SPA
2	SOLV	SOLVIONIC
3	FSU	FRIEDRICH-SCHILLER-UNIVERSITAT JENA
4	SKL	SKELETON TECHNOLOGIES OU
5	TCD	THE PROVOST, FELLOWS, FOUNDATION SCHOLARS & THE OTHER MEMBERS OF BOARD, OF THE COLLEGE OF THE HOLY & UNDIVIDED TRINITY OF QUEEN ELIZABETH NEAR DUBLIN
6	TUD	TECHNISCHE UNIVERSITAET DRESDEN
7	UNISTRA	UNIVERSITE DE STRASBOURG
8	SM	SKELETON MATERIALS GMBH
9	UNR	UNIRESEARCH BV
10	CNR	CONSIGLIO NAZIONALE DELLE RICERCHE
11	UCAM	THE CHANCELLOR MASTERS AND SCHOLARS OF THE UNIVERSITY OF CAMBRIDGE
12	CU	Y CARBON LLC

This project has received funding from the European Union's Horizon Europe research and innovation programme under grant agreement No 101091572. Views and opinions expressed are however those of the author(s) only and do not necessarily reflect those of the European Union. Neither the European Union nor the granting authority can be held responsible for them.

10 Appendix A - Quality Assurance Review Form

The following questions should be answered by all reviewers (WP Leader, reviewer, Project Coordinator) as part of the Quality Assurance procedure. Questions answered with NO should be motivated. The deliverable author will update the draft based on the comments. When all reviewers have answered all questions with YES, only then can the Deliverable be submitted to the EC.

NOTE: This Quality Assurance form will be removed from Deliverables with dissemination level "Public" before publication.

Question	WP Leader	Reviewer	Project Coordinator
	Artur Ciesielski (UNISTRA)	Sebastiano Bellani (BED)	Francesco Bonaccorso (BED)
1. *Do you accept this Deliverable as it is?*	Yes	Yes	Yes
2. *Is the Deliverable complete?* - *All required chapters?* - *Use of relevant templates?*	Yes	Yes	Yes
3. *Does the Deliverable correspond to the DoA?* - *All relevant actions preformed and reported?*	Yes	Yes	Yes
4. *Is the Deliverable in line with the GREENCAP objectives?* - *WP objectives* - *Task Objectives*	Yes	Yes	Yes
5. *Is the technical quality sufficient?* - *Inputs and assumptions correct/clear?* - *Data, calculations, and motivations correct/clear?* - *Outputs and conclusions correct/clear?*	Yes	Yes	Yes
6. *Is created and potential IP identified and are protection measures in place?*	Yes	Yes	Yes
7. *Is the Risk Procedure followed and reported?*	Yes	Yes	Yes
8. *Is the reporting quality sufficient?* - *Clear language* - *Clear argumentation* - *Consistency* - *Structure*	Yes	Yes	Yes